Research Article

Microstructural and small-scale characterization of additive manufactured AlSi10Mg alloy

F. Alghamdi[1] · M. Haghshenas[1]

Abstract
Additive manufacturing of aluminum alloys is considered a promising layer-wise manufacturing method which can produce lightweight critical automotive/aerospace/military components with enhanced physical and mechanical properties. This paper aims at assessing the correlation between microstructure and small-scale characteristics of an additive manufactured AlSi10Mg alloy in the as-printed and heat treated conditions. Depth-sensing nanoindentation testing, as a non-destructive, robust, and convenient testing approach, along with microstructural assessments, using optical microscopy and scanning electron microscopy, were employed to compare the nano-hardness of the printed (selective laser melting method) and the heat treated (age-hardening) materials. Considering the distance from the build plate, a gradation in the cooling rate, and therefore the microstructure, is expected which directly affect the nano-hardness gradient along the deposition direction. Results show a transition in the microstructure from cellular grains, with coral-like silicon fiber colonies, to fragmented/spheroidized eutectic silicon particles upon the heat treatment. Unlike conventionally manufactured AlSi10Mg alloys, upon aging heat treatment in the additive manufactured AlSi10Mg alloy, the nano-hardness is decreased which is mainly contributed to stress relief, elimination of solid solution strengthening, and silicon spheroidization phenomena. These are considered in detail in the current paper.

Keywords Additive manufacturing · AlSi10Mg · Heat treatment · Si spheroidization · Nano-hardness · Nanoindentation

1 Introduction

Additive manufacturing (AM) is considered low waste, and economical for small specified production where it is a technique that could be comparable with the mold casting in the manufacturing of aluminum-made component for various applications and industries [1]. Among various aluminum alloys, cast AlSi10Mg alloy, a hypoeutectic alloy in the Al–Si–Mg system, is the most commonly employed aluminum alloy toward additive manufacturing [2–5]; this is presumably due to the ease of processing and short solidification range (*i.e.* $\Delta T = 40$ K, see Fig. 1) [4, 6]. The alloy is used in fabrication of machine parts, rocker arms, timing gears, compressor cases, fuel pumps, air compressor pistons, aerospace components, high speed rotating parts, crankcases, and engine cooling fans. This near-eutectic alloy comprises aluminum alloyed with silicon of mass fraction up to 10%, small quantities of magnesium and iron, along with other minor elements. Addition of silicon and magnesium elements increases the strength of the cast at ambient and elevated temperatures. They also make the alloy to be more responsive to the heat treatment.

Considering completely different cooling rate in the conventionally cast AlSi10Mg and the additive manufactured counterpart, the produced microstructure and therefore the mechanical properties would alter largely [7]. For instance, what happens in the additive manufacturing (*i.e.,* selective laser melting, SLM) of the AlSi10Mg alloy is localized rapid heating and cooling cycles (*i.e.* 10^6–10^8 °C/s

✉ M. Haghshenas, meysam.haghshenas@engr.und.edu | [1]Department of Mechanical Engineering, University of North Dakota, Grand Forks, ND, USA.

SN Applied Sciences (2019) 1:255 | https://doi.org/10.1007/s42452-019-0270-5

Received: 4 December 2018 / Accepted: 17 February 2019 / Published online: 21 February 2019

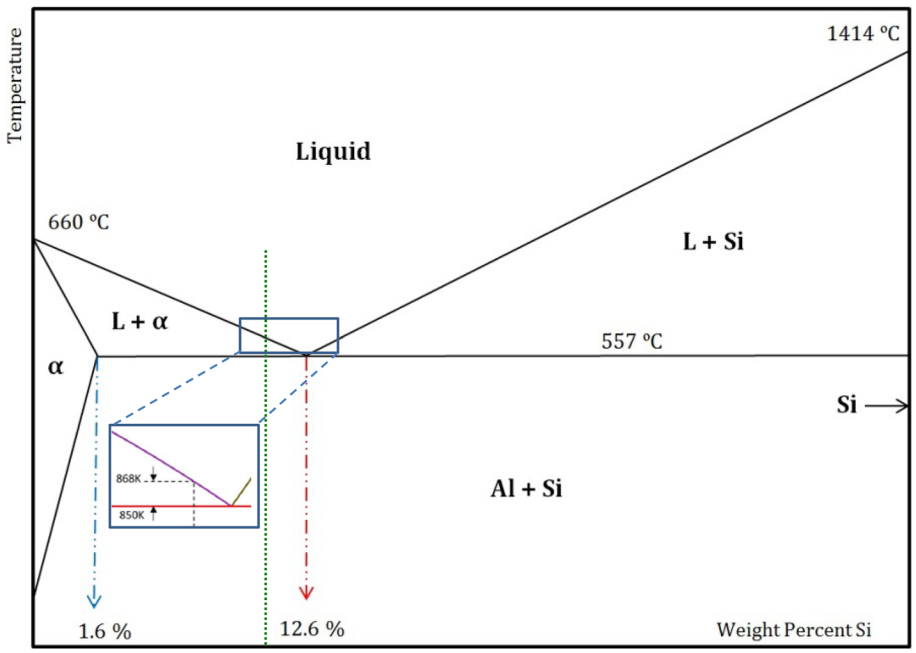

Fig. 1 Al-Si phase diagram and the position of AlSi10Mg alloy [2]

[8]) induced by the SLM process which is not necessarily the case in the conventional casting.

Cast AlSi10Mg alloys are usually treated through T_6 heat treatment. The process includes several hours of solution heat treatment which is followed by quenching in water and subsequently aging at moderate temperatures. This heat treatment produces the strengthening precipitates of Mg_2Si in the alloy which improves the ductility and strengthens the aluminum matrix. Recently some papers have been published on T_6 heat treatment of the additive manufactured AlSi10Mg alloy [3, 9–15].

Li et al. [3] studied the effect of heat treatment on AlSi10Mg alloy fabricated by selective laser melting. They reported a tangible decrease (− 61%) in the tensile strength in the T_6 heat tread material as compared with the as-printed alloy. Takata et al. [13] studied the change in the microstructure of the additive manufactured AlSi10Mg due to heat treatment. They reported the following sequence in the microstructure induced by the heat treatment, (i) recovery, (ii) silicon spheroidization and coarsening, (iii) formation of a stable intermetallic phase (AlFeSi). Aboulkhair et al. [9, 16] studied the microstructure and mechanical properties of the SLM AlSi10Mg alloy. They reported softening of the SLM AlSi10Mg alloy as well. Brandl et al. [17] assessed the fatigue performance of the T_6 heat treated SLM AlSi10Mg and reported enhanced fatigue life in the heat treated material as compared with the as-printed alloy.

Zhuo et al. [18] assess the effect of post-process heat treatment on microstructure and mechanical properties of additive manufactured AlSi10Mg alloy. They studied various heat treatments and employed nanoindentation to evaluate the effect of heat treatments on the phase constituents, microstructure, residual stress and mechanical properties of the laser additive manufactured AlSi10Mg alloy. They concluded that 300 °C/2 h + water quench is an effective heat treatment which provide enhanced mechanical properties and eliminates most of the residual stresses of the SLM AlSi10Mg alloy.

Aboulkhair et al. [19], using a nanoindentation testing approach, assessed nano, micro, and macro properties of selective laser melted AlSi10Mg. They observed uniform nano-hardness in the SLM material, compared with the cast counterparts. They attributed this to fine microstructure and good distribution of Si at the grain boundaries due to faster cooling rate.

In a separate study Aboulkhair et al. [9] studied the effect of a conventional T6-like heat treatment on microstructure and mechanical properties, assessed by a nanoindentation testing technique, of selectively laser melted AlSi10Mg alloy. Unlike T6 heat treatment in the cast Al–Si parts, they observed a drop in the nano-hardness upon T6 treatment in the as-printed samples. They attributed this phenomenon to change in the strengthening mechanisms and Si spheroidization. In a follow up study, Aboulkhair et al. [16] evaluated microstructure and nano-mechanical properties of additive manufactured AlSi10Mg. They employed nanoindentation and energy dispersive x-ray (EDX) to create hardness profile and their correlations with the chemical composition across the melt pool of the printed samples. They observed a uniform nano-hardness distribution with no spatial variation across the SLM material.

Everitt et al. [20] employed nanoindentation and showed uniform local mechanical properties across melt pools and layers produced by selective laser melting of AlSi10Mg alloy. They attributed the uniform nano-hardness profile to the highly fine microstructure accompanied with the enhanced dispersion of the alloying elements.

Despite mentioned papers on the heat treatment of the SLM AlSi10Mg alloy, detailed and atomic scale mechanism of silicon spheroidization induced by the heat treatment as well as the micromechanical response of the alloy have not been studied. Considering the fact there exists gradation in microstructure (and therefore) mechanical properties of the additive manufactured AlSi10Mg alloy [21–23], instrumented depth sensing indentation is a reliable, convenient and robust method to track the changes in local mechanical properties and extract some fundamental characteristics, *i.e.* dislocation activities, indentation size effect, etc., especially when a small volume of materials is available. This paper explores and compares micromechanical properties (*i.e.* nanohardness, reduced modulus, indentation size effect) of an SLM AlSi10Mg alloy in the as printed and the T_6 heat treated at the nano/micro-levels.

2 Experimental procedure

The AlSi10Mg samples (cubes of 1 cm^3) were produced from atomized powders using an SLM 280 printer with two 400-watt lasers at CalRAM Inc. The AlSi10Mg test samples were built according to the default SLM 280 parameter set. To avoid oxidation, the printing operation was performed in an inert argon atmosphere. Upon printing, the cubes were cut from the aluminum substrate using electron discharge machining (EDM). A separate set of as-printed samples were employed toward T_6 heat treatment. This includes solutionizing at 520 °C for 1 h, the water quenching, and the artificial ageing at 170 °C for 4 h.

Upon completion of the heat treatment cycle, both as-printed and heat treated specimens were mechanically (up to 4000# sandpaper to remove the surface oxidations and contaminations) and chemically polished to get scratch free mirror-like surfaces. At this stage samples were etched using Keller's reagent (2.5% HNO_3, 1% HF, 1.5% HCl, 95% distilled water) to assess the microstructure of the materials using optical microscopy (metallurgical light microscope model MM 500T) and scanning electron microscopy (SEM model FEI FEG 650).

To establish the correlations between the microstructure and the mechanical properties (*i.e.* nano-hardness and reduced modulus), an instrumented (depth-sensing) nanoindentation system was employed (Hysitron Ubi-1 Nanoindenter) equipped with a self-similar pyramidal Berkovich indenter. Tests were performed under load-controlled mode with the peak load of 9.5 mN with the load rate of 1 mN/s and spacing of 400 µm with total of 25 indents were performed on both XY and YZ planes where XY starts and ends from one side edge to the other one and YZ starts near the substrate and ends up neat the top of the sample. Upon reaching the pre-set peak load, the load is held constant for 2 s then the sample is unloaded. Indentation load (P), indentation depth (h), and time are three main parameters that are recorded during the testing. Using well-known Oliver/Pharr [24] method, indentation stress (σ_{ind}) and reduced modulus are calculated. To confirm the nanoindentation testing results, Vickers hardness measurements (load of 500 g, space of 200 µm with total of 50 indents) was carried out on the both as-printed and heat treated samples as well on both XY and YZ planes.

3 Results and discussion

3.1 Microstructure characterization

Figure 2 presents the optical microscopy images of the as-printed sample. The microstructure has resulted from the high cooling rate experienced by the material during the printing operation. The as-printed sample shows the characteristic cellular microstructure, supersaturated α-Al matrix (dark phase) and continuous fibrous coral shape network of eutectic Si particles (bright phase), of the SLM AlSi10Mg consisting of melt pools with a half-cylindrical shape which correspond with local melting and rapidly solidifying regions. The breakdown of the microstructure shows that it is distinguished into layers. There are sections known as the melt pools that are divided into three distinct regions. These are the heat affected zone, the melt pool boundary, and the melt pool core (see Fig. 2). Due to this layer-based manufacturing approach, the resulting microstructures are usually non-homogenous. The Al cells usually appear finer towards the melt pool core when viewed perpendicular to the build direction. When viewed parallel to the build direction, the Al cells at the melt pool boundaries appear elongated.

Upon heat treatment, the microstructure changes noticeably. Figure 3 shows the microstructure after T_6 heat treatment. The interconnected fibrous coral shape network of silicon disappears and spherical-like silicon particles are uniformly distributed within the α-Al matrix. Figures 4 and 5 show the SEM micrographs of the as-printed and the heat treated material at different magnifications. Considering Fig. 5a, b it is clear that Si particles become larger and more widely spaced because of coalescence and Ostwald ripening (large particles grow at the expense of small particles). Ostwald ripening is thermodynamically

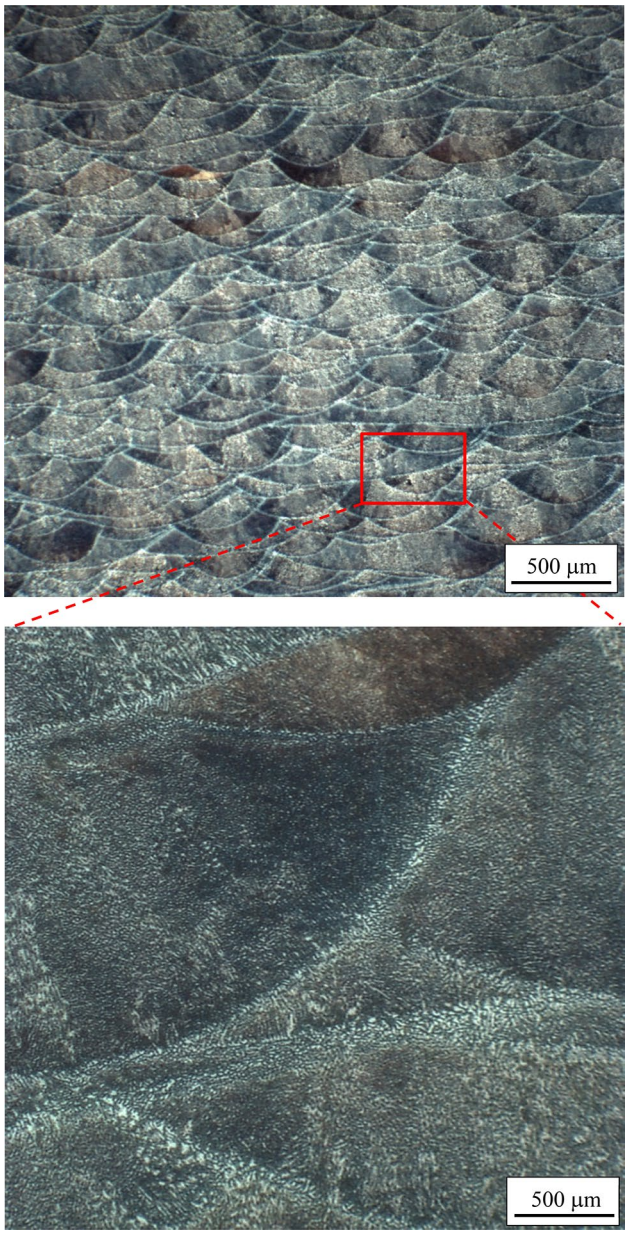

Fig. 2 As-printed cellular microstructure of the AM AlSi10Mg showing melt pool core and the boundaries

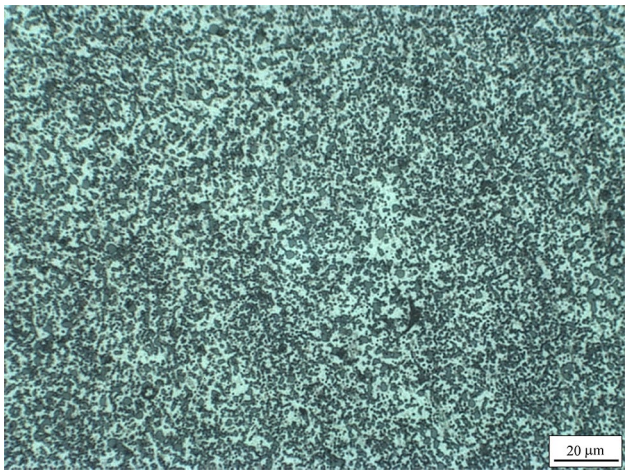

Fig. 3 Micrograph of the heat treated material. Upon conducting the T_6 heat treatment, the Si fibers/needles in the as printed material are converted to round (spheroidized) particles distributed evenly within the Al matrix

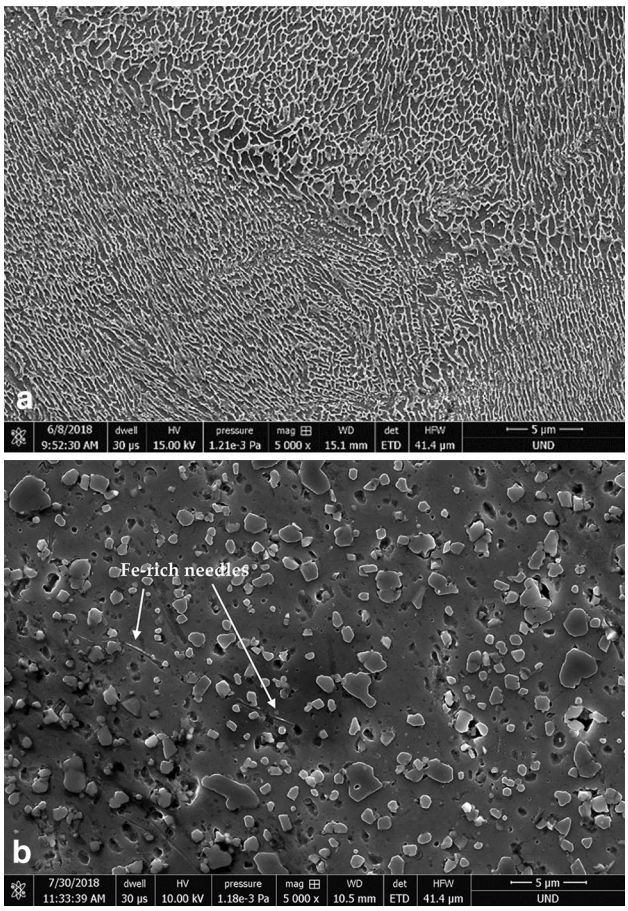

Fig. 4 SEM micrographs of **a** as printed, **b** heat treated structures. It is possible to observe the different sizes of the cellular-dendritic structures. Supersaturated α-Al solid solution are separated by a continuous network of intercellular eutectic silicon

and energetically a spontaneous process which reduces internal energy of a system. Small particles do possess large surface-to-volume ratio which results in high internal energy of the system because of large surface energy. However, when particles grow, this internal energy reduces as surface-to-volume ratio becomes smaller. Having said this, smaller particles on the surface tend to disengage themselves and migrate (diffuse) to the surface of coarser particles.

In the current study, the average size of the spheroidized Si particles is between 0.7 and 1 µm. However,

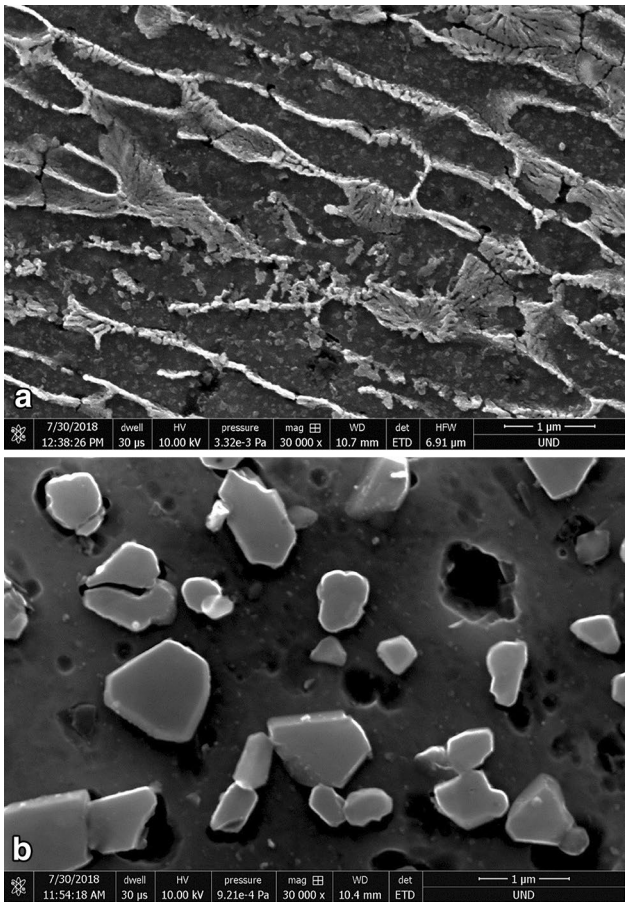

Fig. 5 **a** SEM micrographs of SLM built, **b** SEM micrographs of SLM built samples after heat treatment. Majority of the Si particles appeared to have irregular shape, and their size ranged from approximately 200 nm to 4 µm

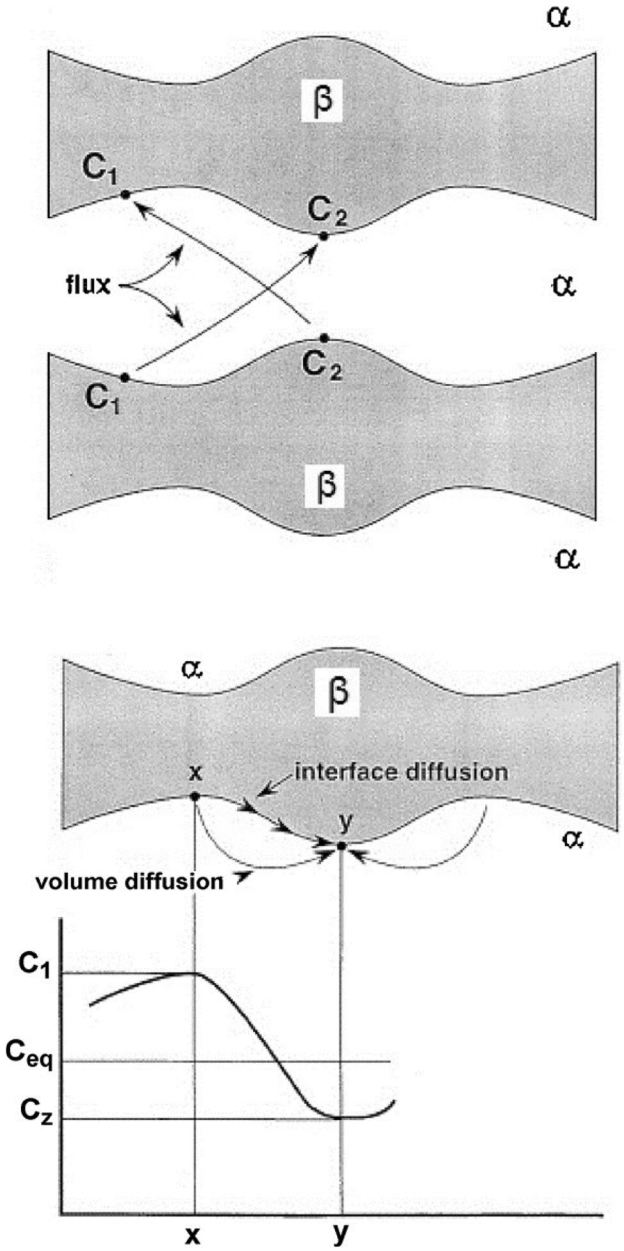

Fig. 6 The schematic representation of volume and interface diffusion resulting in the Si fragmentation and spheroidization [19, 21]

according to Li et al. [3] with increasing the artificial ageing time to 12 h, the Si particles can further grow to a size up to 5 µm. The increase in the size of Si particles indicates that in the as-built SLM sample, the Al matrix is supersaturated and during the heat treatment the excess Si precipitates out.

To better assess the effect of T_6 heat treatment on the Si morphology evolution, the modification mechanisms of these eutectic aggregates need to be well understood. During solution heat treatment, eutectic Si particles are expelled for the α-Al matrix (which is now in the supersaturated state). This results in the segregation of Si particles along the α-Al grain boundaries. Also, coral-like eutectic Si fibers are fragmented and disintegrated at the shape discontinuities/instabilities such as joint of the Si branches and/or necks of the Si crystals [3, 25–27]. Upon the fragmentation of the Si branches, Si spheroidization is driven through surface self-diffusion (the element changes the location by diffusing on the surface) [28] or Al–Si interdiffusion at Si/Al interface (the silicon atoms move through the aluminum at the Si/Al interface). The second scenario (Si/Al interface diffusion) is more energetically promising. Indeed, the chemical potential gradient between the interfacial discontinuities and the adjacent area provides the required energy from the solid-state atomic diffusion and therefore morphological evolution (spheroidization), see Fig. 6. Considering the solid-state atomic diffusion as a time and temperature dependent phenomenon, a heat treatment cycle at an elevated temperature but below eutectic temperature could be an efficient technique to change the shape and morphology of the Si.

Upon providing sufficient time and temperature particle coarsening occurs to reduce the overall energy of the system. That is, the particles become coarse as the aspect ratio reduces leading to loss of the interconnection of the eutectic phases. Temperature and the duration of exposure determine the rate at which interconnectivity is lost. Increase in the percentage of silicon increases the ductility of the materiel.

3.2 Mechanical properties

Figure 7 shows the indentation load/displacement curves of the as-printed and heat treated AlSi10Mg samples. As observed, at a constant load of 9.5 mN, the indenter displacement within the material is less in the as the printed sample as compared with the heat-treated material. This confirms that the heat-treated material is softer than the as-printed one. This is shown in Fig. 8a, b which includes cross-sectional hardness measures (in GPa) for both the as-built and the heat-treated samples in the YZ and XY planes. A clear change in the hardness values of the heat-treated alloy is observed; the average Nano hardness value for as-built materials is 2.71 ± 0.12 GPa whereas the heat treated one shows 1.56 ± 0.11 GPa. This confirms 42% decrease in the strength upon heat treatment. On other hand, the average nano-hardness for the as-printed and the heat treated materials is 2.58 ± 0.12 GPa and 1.59 ± 0.11 GPa, respectively (38% decrease in strength). These results were confirmed upon performing Vickers hardness tests; the average Vickers hardness value on the YZ plane for the as-built and the heat treated materials is 115.7 ± 3.5 and 97.3 ± 2.8, respectively. The average Vickers hardness value on the XY plane for the as-built and the heat treated materials is 112.7 ± 2.4 and 94.4 ± 2.84, respectively.

Considering the microstructure of the as-printed AlSi10Mg (Figs. 2, 4a, and 5a), the alloy can be considered as a "natural" metal matrix composite with α-Al as the matrix and interconnected coral-like Si fibers as reinforcement phase. Having said this, the main mechanisms that contribute to the strengthening of the as-printed sample include grain boundary strengthening due to the presence of a cellular structure (Hall–Petch effect), solid-solution strengthening due to the presence of Mg and Si elements, dislocation strengthening due to large dissimilarities between coefficient of thermal expansion between α-Al (13.1×10^{-6} m/m. °C) and Si coral-like fibers (2.8×10^{-6} m/m. °C), and finally load transfer from matrix to the Si fibers [30, 31].

Upon heat treatment, some of the mentioned strengthening contributions are weakened or eliminated. The decrease in the strength of the heat treated material can then be attributed to change in the morphology of the eutectic Si from fibrous to spheroidized, grain coarsening due to solution heat treatment, and reduction of solid-solution strengthening. Indeed, the 1-h solution heat

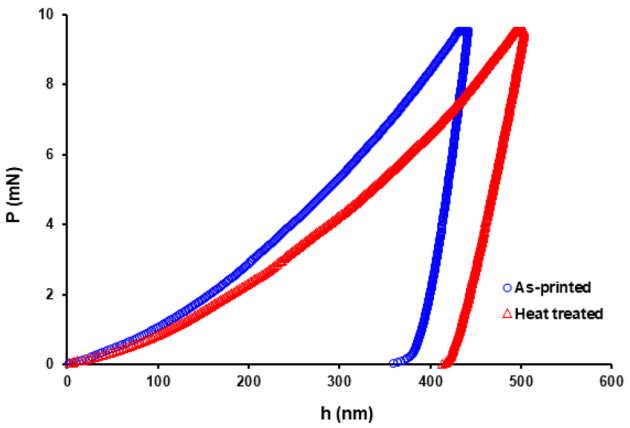

Fig. 7 Indentation load/displacement curves of as printed and heat treated materials

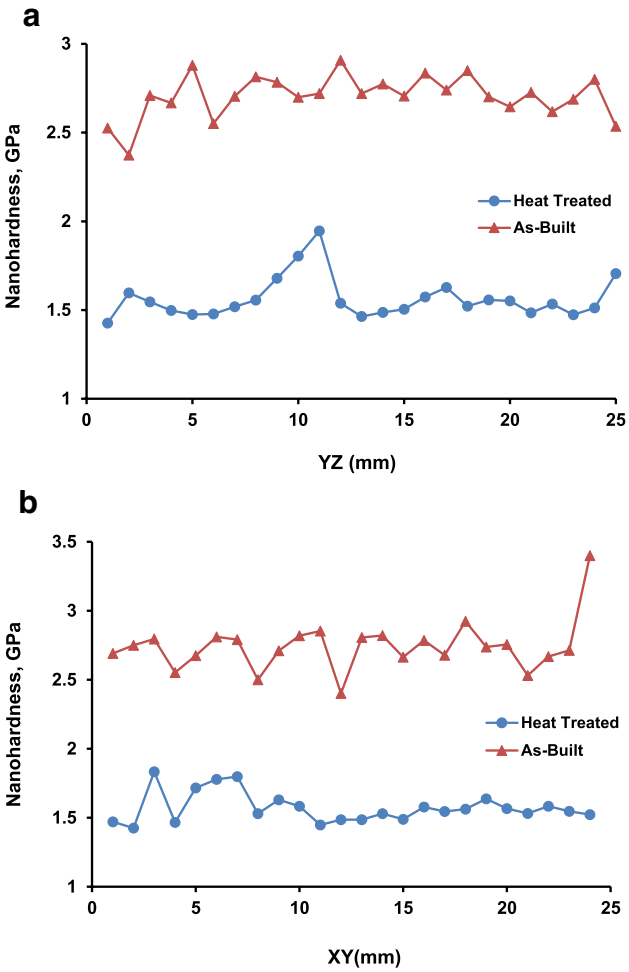

Fig. 8 Nano-hardness measurement for AlSi10Mg, **a** YZ plane, **b** XY plane

treatment at 520 °C provides sufficient time and temperature (driving force) for the interconnected Si fibers to be transformed to the Si particles (spheroids) along with α-Al grain growth. These phenomena directly result in reduced strength in the heat-treated materials. The artificial ageing at 170 °C for 4 h results in Mg_2Si precipitation and Orowan strengthening, however, it seems that the mentioned softening mechanisms overcome the strengthening effect of the Mg_2Si precipitates [13, 23, 32–34]. This could be the main difference between conventionally made and additively manufactured AlSi10Mg alloy with regard to the response of the material to the T_6 artificial ageing heat treatment. In the conventionally manufactured AlSi10Mg alloy, artificial ageing results in the formation and homogeneous distribution of β′ (Mg_2Si) precipitates which contribute significantly to the strengthening of the material [35].

To get some information on the effect of heat treatment on the yield strength of the materials, Vickers hardness testing was performed. Figure 9 on the samples and the following correlation, between yield strength (σ_{yield}) and Vickers hardness, suggested by Cahoon et al. [36] were employed:

$$\sigma_{yield} = \left(\frac{VH}{3}\right)(0.1)^n \quad (1)$$

where VH is Vickers hardness in MPa ($VH_{MPa} = VHN \times 9.807$). n is the strain hardening coefficient selected are 0.2 and 0.1, for the as-printed and the heat treated AlSi10Mg materials, respectively [12, 14]. Considering this equation, the average yield strength for the as-printed and heat treated materials are 245.1 MPa and 188.7 MPa, respectively. This is in agreement with the hardness results reported by Zhou et al. [12] and σ_{yield} from tensile tests for the SLM AlSi10Mg alloys [3, 37].

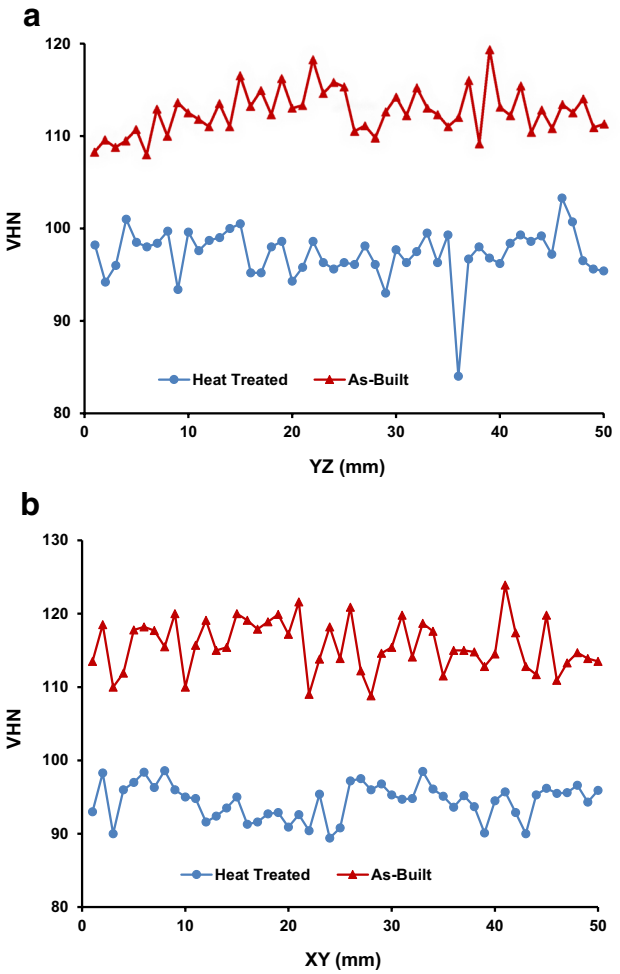

Fig. 9 Vickers hardness measurement for AlSi10Mg, **a** YZ plane, **b** XY plane

3.3 Depth-dependent indentation stress

We are interested in assessing the relationship between nanoindentation hardness and the indentation depth to see if there is any indentation size effect and if so how this varies in the as printed and the heat treated materials. To do so, we first need to calculate the indentation stress using Eq. 2 [38]:

$$\sigma_{ind} = \frac{P}{24.56 \times (h_{ind} + 0.06R)^2} \quad (2)$$

where R is the Berkovich tip radius (100 nm for the indenter used in this study), P is the indentation load, and h_{ind} is the indentation contact depth. It should be noted that indentation stress (σ_{ind}) is different from the indentation hardness values. This is because indentation stress includes both the elastic and the plastic depth in the calculated indentation area, while the conventional indentation harness is calculated with the residual plastic indentation area [39].

Figure 10 shows the indentation stress versus indentation depth in the as-printed and heat treated materials. As observed, indentation stress is dependent upon depth (σ_{ind} increases with the decrease in the indentation depth). That is shallow-depth indentation results in higher hardness as compared with large-depth ones (Fig. 11). This trend cannot necessarily be justified with classical plasticity. This effect cannot either be solely justified with the indenter and/or sample artificial effects like indenter blunting, surface oxidation, surface deformation layers, etc. There are some real physical phenomena behind this trend. The observed increase in the indentation stress at shallower indentation depths is attributed to dislocation starvation and strain gradient plasticity [23, 31–42].

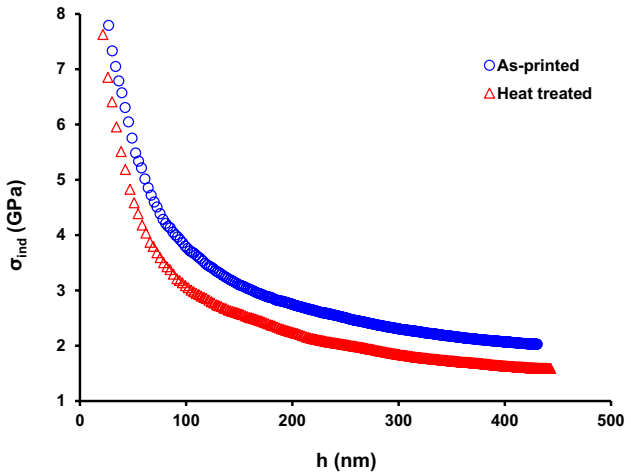

Fig. 10 Indentation size effect in the as-printed and heat treated materials

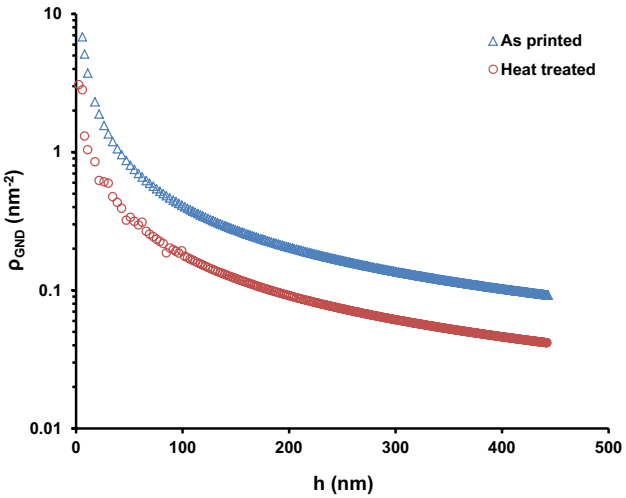

Fig. 12 Density of GNDs versus depth in the as-printed material

At the earliest stages of the nanoindentation when indenter's tip contacts the surface of the material with a depth of indentation only a few nanometers, the material can be considered dislocation-free (so-called dislocation starved) as there is no physical room for dislocations to be generated. Here the strength of the material can be as big as the theoretical strength. When indenter further drives within the material (but still in the nanometer depths), an extra storage of dislocations (geometrically necessary dislocations, GNDs) is introduced in the material in order to provide the necessary lattice rotation to accommodate the shape of the indenter (this is shown schematically in Fig. 12). As the indentation is shallow, the plastic deformation is forced to occur over a very small volume of martial containing a limited number of easy slip systems. Therefore, the GNDs may have different mobility and Burger's vector as compared with ordinary (statistically stored) dislocations. They may also be forced to move on non-easy slip systems. The density of the GNDs is inversely related with indentation depth; that is, at shallow depths larger population of GNDs is expected which results in the enhanced strength near the surface of the sample. The density of ρ_{GNDs} can be described as follows [43, 44]:

$$\rho_{GNDs} = \frac{3}{2bh}\tan^2(\theta) \tag{3}$$

where $\theta = 70.32°$ and represents the effective semi-angle of the conical indenter equivalent to the Berkovich one, b is Burgers vector (2.86×10^{-10} m for aluminum), and h is the contact depth. Figure 12 shows the plot of ρ_{GNDs} versus indentation depth. As seen, the density of GNDs increases with decreasing in the indentation depth and this directly contributes to the strain gradient near the surface of the sample. At large depths through a balance between work hardening effect (dislocation generation and multiplication) and dynamic recovery (large volumes experiencing high stresses). Therefore, indentation stress (hardness)

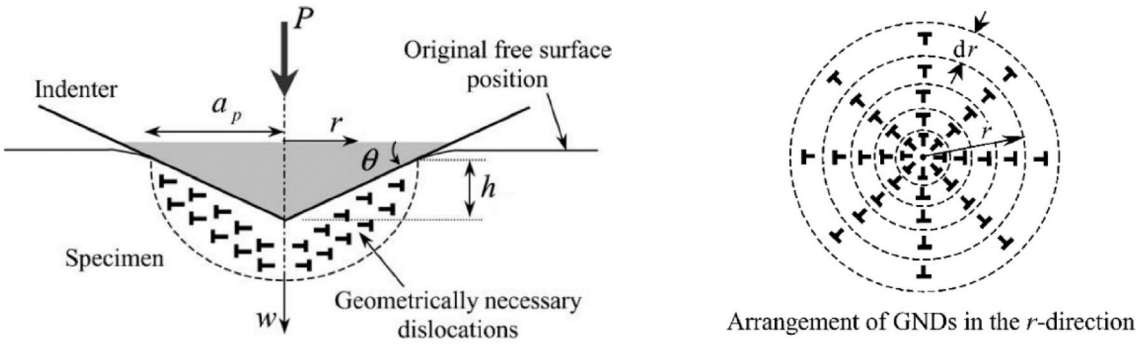

Fig. 11 Schematic representation of geometrically necessary dislocations (GNDs) created during the indentation process. The dislocation structure is idealized as circular dislocation loops [33]

approaches a constant value as an equilibrium between different acting processes is reached. In the present study, the size effect is observed in both as-printed and heat-treated sample, however, the effect is more pronounced in the as-printed material. This is because of less strength in the heat-treated material.

4 Conclusion

Employing an instrumented nanoindentation technique, micromechanical responses of an additive manufactured AlSi10Mg in the as-printed and heat treated conditions were elaborated. This was coupled with microstructural (OM and SEM) evidence to establish microstructure/micromechanical correlations. Here is a list of main findings of the present paper:

1. In the studied AM AlSi10Mg, the T_6 artificial ageing resulted in a 42% decrease in the strength upon heat treatment through the results from the nanoindentaion tests.
2. Drop in the strength upon heat treatment confirms that Orowan strengthening effect induced by Mg_2Si precipitates is dominated by some softening effects mainly Si spheroidization, grain growth, and elimination of solid-solution strengthening. This is not the case in the artificial ageing of conventionally cast AlSi10Mg.
3. Indentation size effect, increase in hardness with the decrease in the depth, is observed in both as-printed and heat treated materials. Since the heat-treated material is softer than the as-printed one, the indentation size effect in the heat treated alloy is less pronounced.

Compliance with ethical standards

Conflict of interest The authors declare that they have no conflict of interests.

References

1. Syed AM, Tofail EP, Koumoulos Bandyopadhyay A, Bose S, O'Donoghue L, Charitidis C (2018) Additive manufacturing: scientific and technological challenges, market uptake and opportunities. Mater Today 21:22–37
2. Jordović B, Nedeljković B, Mitrović N, Živanić J, Maričić A (2014) Effect of heat treatment on structural changes in metastable AlSi10Mg alloy. J Min Metall Sect B Metall 50(2):133–137
3. Li W, Li S, Li J, Zhang A, Zhou Y, We Q, Yan C, Shi Y (2016) Effect of heat treatment on AlSi10Mg alloy fabricated by selective laser melting: microstructure evolution, mechanical properties and fracture mechanism. Mater Sci Eng A 663:116–125
4. Louvis E, Fox P, Sutcliffe CJ (2011) Selective laser melting of aluminium components. J Mater Process Technol 211(2):275–284
5. Iturrioz A, Gil E, Petite MM, Garciandia F, Mancisidor AM, San Sebastian M (2018) Selective laser melting of AlSi10Mg alloy: Influence of heat treatment condition on mechanical properties and microstructure. Weld World 62:885–892
6. Kempen K, Thijs L, Van Humbeeck J, Kruth J-P (2012) Mechanical properties of AlSi10Mg produced by selective laser melting. Phys Procedia 39(2012):439–446
7. Biffi CA, Fiocchi J, Tuissi A (2018) Selective laser melting of AlSi10Mg: Influence of process parameters on Mg2Si precipitation and Si spheroidization. J Alloys Compd 755:100–107
8. Li Y, Gu D (2014) Parametric analysis of thermal behavior during selective laser melting additive manufacturing of aluminum alloy powder. Mater Des 63:856–867
9. Aboulkhair NT, Maskery I, Tuck C, Ashcroft I, Everitt NM (2016) The microstructure and mechanical properties of selectively laser melted AlSi10Mg: the effect of a conventional T6-like heat treatment. Mater Sci Eng A 667:139–146
10. Liu X, Beausir B, Zhang Y, Gan W, Yuan H, Yu F, Esling C, Zhao X, Zuo L (2018) Heat-treatment induced defect formation in α-Al matrix in Sr-modified eutectic Al–Si alloy. J Alloys Compd 730:208–218
11. Li J, Cheng X, Liu D, Zhang SQ, Li Z, He B, Wang HM (2018) Phase evolution of a heat-treatable aluminum alloy during laser additive manufacturing. Mater Lett 214:56–59
12. Fiocchi J, Tuissi A, Bassani P, Biffi CA (2017) Low temperature annealing dedicated to AlSi10Mg selective laser melting products. J Alloys Compd 695:3402–3409
13. Takata N, Kodaira H, Sekizawa K, Suzuki A, Kobashi M (2017) Change in microstructure of selectively laser melted AlSi10Mg alloy with heat treatments. Mater Sci Eng A 704:218–228
14. Zhou L, Mehta A, Schulz E, McWilliams B, Cho K, Sohn Y (2018) Microstructure, precipitates and hardness of selectively laser melted AlSi10Mg alloy before and after heat treatment. Mater Charact 143:5–17
15. Fousováa M, Dvorský D, Michalcová A, Vojtěch D (2018) Changes in the microstructure and mechanical properties of additively manufactured AlSi10Mg alloy after exposure to elevated temperatures. Mater Charact 137:119–126
16. Aboulkhair NT, Maskery I, Tuck C, Ashcroft I, Everitt NM (2016) On the formation of AlSi10Mg single tracks and layers in selective laser melting: Microstructure and nano-mechanical properties. J Mater Process Technol 230:88–98
17. Brandl E, Heckenberger U, Holzinger V, Buchbinder D (2012) Additive manufactured AlSi10Mg samples using Selective Laser Melting (SLM): microstructure, high cycle fatigue, and fracture behavior. Mater Des 34:159–169
18. Zhuo L, Wang Z, Zhang H, Yin E, Wang Y, Tao X, Li C (2019) Effect of post-process heat treatment on microstructure and properties of selective laser melted AlSi10Mg alloy. Mater Lett 234:196–200
19. Aboulkhair NT, Stephens A, Maskery I, Tuck C, Ashcroft I, Everitt NM (2015) Mechanical properties of selective laser melted AlSi10Mg: nano, micro, and macro properties. In: Solid freeform fabrication symposium 2015. Austin, Texas, pp 1026–1036
20. Everitt NM, Aboulkhair NT, Maskery I, Tuck C, Ashcroft I (2016) Nanoindentation shows uniform local mechanical properties across melt pools and layers produced by selective laser melting of AlSi10Mg alloy. Adv Mater Lett 7:13–16
21. Liu YJ, Liu Z, Jiang Y, Wang GW, Yang Y, Zhang LC (2018) radient in microstructure and mechanical property of selective laser melted AlSi10Mg. J Alloy Compd 735:1414–1421

22. Chen Bo, Yao Yongzhen, Song Xiaoguo, Tan Caiwang, Cao Liang, Feng Jicai (2018) Microstructure and mechanical properties of additive manufacturing AlSi10Mg alloy using direct metal deposition. Ferroelectrics 523:153–166. https://doi.org/10.1080/00150193.2018.1392147
23. Trevisan Francesco, Calignano Flaviana, Lorusso Massimo, Pakkanen Jukka, Aversa Alberta, Ambrosio EP, Lombardi M, Fino P, Manfredi D (2017) On the selective laser melting (SLM) of the AlSi10Mg alloy: process, microstructure, and mechanical properties. Materials 10:76. https://doi.org/10.3390/ma10010076
24. Oliver WC, Pharr GM (1992) An improved technique for determining hardness and elastic modulus using load and displacement sensing indentation experiments. J Mater Res 7(6):1564–1583
25. E Ogris (2002) Institute of Metallurgy, ETH Zürich Ph.D. Thesis
26. Wang RY, Lu WH, Metall S (2013) Spheroidization of eutectic silicon in direct-electrolytic Al-Si Alloy. Mater Trans A 44:2799–2809
27. Ogris E, Wahlen A, L€uchinger H, Uggowitzer PJ (2002) On the silicon spheroidization in Al–Si alloys. J Light 2:263–269
28. Keeffe ME, Umbach CC, Blakely JM (1994) Surface self-diffusion on Si from the evolution of periodic atomic step arrays. J Phys Chem Solids 55:965–973
29. Chaudhury SK, Apelian D (2006) Effects of rapid heating on aging characteristics of T6 tempered Al–Si–Mg alloys using a fluidized bed. J Mater Sci 41:4684–4690
30. Taufik RS, Sulaiman S (2013) Thermal expansion model for cast aluminium silicon carbide. Procedia Eng 68:392–398
31. Ma K, Wen H, Hu T, Topping TD, Isheim D, Seidman DN, Lavernia EJ, Schoenung JM (2014) Mechanical behavior and strengthening mechanisms in ultrafine grain precipitation-strengthened aluminum alloy. Acta Mater 62:141–155
32. Aboulkhair NT, Tuck C, Ashcroft I, Maskery I, Everitt NM (2015) On the precipitation hardening of selective laser melted AlSi10Mg. Metall Mater Trans A 46:3337–3341
33. Casati R, Coduri M, Tirelli V, Vedani M, Nasab MH (2018) Effects of platform pre-heating and thermal-treatment strategies on properties of alsi10mg alloy processed by selective laser melting. Metals 8:954. https://doi.org/10.3390/met8110954
34. Xianglong Yu, Wang L (2018) T6 heat-treated AlSi10Mg alloys additive-manufactured by selective laser melting. Procedia Manuf 15:1701–1707
35. Sjölander E, Seifeddine S (2010) Artificial ageing of Al–Si–Cu–Mg casting alloys. J Mater Process Technol 210:1249–1259
36. Cahoon J, Broughton W, Kutzak A (1971) The determination of yield strength from hardness measurements. Metall Mater Trans B Process Metall Mater Process Sci 2:1979–1983
37. Tradowsky U, White J, Ward R, Read N, Reimers W, Attallah M (2016) Selective laser melting of AlSi10Mg: Influence of post-processing on the microstructural and tensile properties development. Mater Des 105:212–222
38. Muhammad M, Masoomi M, Torries B, Shamsaei N, Haghshenas M (2018) Depth-sensing time-dependent response of additively manufactured Ti-6Al-4V alloy. Addit Manuf 24:37–46
39. Bhakhri V, Klassen RJ (2009) The strain-rate dependence of the nanoindentation stress of gold at 300 K: A deformation kinetics-based approach. J Mater Res 24:1456–1465
40. Greer JR, Nix WD (2006) Nanoscale gold pillars strengthened through dislocation starvation. Phys Rev B 73:245410
41. Nix WD, Greer JR, Feng G, Lilleodden ET (2007) Deformation at the nanometer and micrometer length scales: Effects of strain gradients and dislocation starvation. Thin Solid Films 515(6):3152–3157
42. Greer JR, Oliver WC, Nix WD (2005) Size dependence of mechanical properties of gold at the micron scale in the absence of strain gradients. Acta Mater 53:1821–1830
43. Voyiadjis GZ, Yaghoobi M (2017) Review of nanoindentation size effect: experiments and atomistic simulation. Crystals 7(32):1. https://doi.org/10.3390/cryst7100321
44. Nix WD, Gao H (1998) Indentation size effects in crystalline materials: a law for strain gradient plasticity. J Mech Phys Solids 46:411–425